ingegneria sismica
International Journal of Earthquake Engineering
Anno XLIII - Num. 2 - 2026

Optimal Model Design for Distributed Photovoltaic Dispatch Systems in Uncertain Load Environments and Generation of Diffusion Model Control Strategies

Xiran Zhang[1,*], *Xuehao He*[1], *Yiran Rao*[2], *JiaquanYang*[1] *and Junyu Liang*[1]

[1] Yunnan Electric Power Research Institute, Kunming, Yunnan, 650217, China
[2] Shenzhen Kezhongyun Technology Co., LTD., Shenzhen, Guangdong, 518000, China

SUMMARY: *To address the issue of uncertain load conditions in photovoltaic power generation systems, this paper proposes an adaptive robust optimization scheduling model and microgrid operation control strategy. The method first uses GPR adaptive generation to obtain the mean and variance of the day-ahead power output forecast values, and introduces key data features from the forecast stage to reduce the error in the robust optimization uncertainty set. Subsequently, the proposed multi-state ant colony-bacterial foraging algorithm can achieve maximum power point tracking (MPPT) for the photovoltaic system under PSC conditions. In the case study analysis, the total operating cost of the proposed model is 309,200 yuan lower than that of the classical two-stage robust optimization model, validating that the proposed adaptive robust optimization model better balances the operational economic advantages during microgrid optimization scheduling. Additionally, the maximum power value tracked by the algorithm under the given conditions is 732.6 W, with an error of only 0.01 W compared to the actual maximum power. This verifies that the proposed algorithm has the advantages of fast optimization speed and very small system steady-state oscillations.*

KEYWORDS: *multi-mode ant colony-bacterial foraging algorithm; robust optimization; photovoltaic power generation; microgrid*

1 Introduction

With the continuous growth of global energy demand and the increasing awareness of environmental protection, the development and utilization of renewable energy have become a strategic priority for countries worldwide [1, 2]. Among these, distributed photovoltaic power generation has garnered significant attention and application due to its clean, renewable, and widely distributed characteristics [3]. However, the large-scale integration of distributed photovoltaic systems has profound implications for power grids. The large-scale integration of distributed PV into medium- and low-voltage distribution grids has led to issues such as voltage over-limiting, feeder overloading, and line protection failures, posing challenges to the safe and stable operation of distribution grids [4, 5]. Additionally, the randomness and intermittency of PV output, coupled with the emergence of numerous new types of loads, have significantly increased the uncertainty in distribution grid operations, making the grid more complex and unpredictable [6, 7]. How to effectively address these impacts and ensure the safe and stable operation of the power grid has become an urgent issue to be resolved.

To address the challenges posed by distributed photovoltaic power generation, power grid

---

*zhangxiran0513@163.com

https://doi.org/10.65102/is2026717

dispatch and management technologies need to be continuously innovated, and the construction and application of intelligent dispatch systems have become critical [8]. By integrating advanced information technology, big data analysis, and artificial intelligence algorithms, intelligent dispatch systems can monitor grid operational status in real time, predict PV power generation output trends, and adjust grid dispatch strategies accordingly to ensure stable grid operation [9-12]. Additionally, intelligent dispatch systems can enable information exchange and coordinated control between PV power sources and the grid, enhancing overall grid operational efficiency. The application of these technologies provides strong support for the intelligent and efficient operation of power grids [13-16]. Therefore, with the increasing proportion of renewable energy sources connected to the grid, it is necessary to consider uncertain load conditions when evaluating the system. By quantifying the maximum distributable photovoltaic installation capacity that the distribution grid can withstand under safety operation constraints, the distribution grid can be managed through scheduling to enhance its capacity to accommodate distributed photovoltaic power generation [17-19].

In recent years, researchers both domestically and internationally have conducted studies and explorations on optimization dispatch strategies for photovoltaic systems in distribution grids. Literature [20] established a probabilistic optimal power flow (P-OPF) model to represent the impact of photovoltaic distributed generators (PV-DG) power and load uncertainties on microgrid day-ahead dispatch, and utilized an improved Harr two-point estimation method to solve the model, thereby obtaining the range of changes in microgrid day-ahead dispatch solutions. Reference [21] indicates that renewable energy sources such as solar photovoltaic and wind power exhibit fluctuating and uncertain characteristics. It proposes a multi-objective wind-driven optimization (MOWDO) algorithm to solve multi-objective energy optimization problems in smart grids, providing effective support for grid load balancing and distributed energy scheduling. Literature [22] investigates multi-timescale optimization scheduling strategies for microgrids under uncertain source-load conditions. A two-stage distributed robust optimal scheduling model is applied to analyze the optimal scheduling solution during the day-ahead scheduling phase, while an intraday rolling optimization and real-time adjustment optimization scheduling model is constructed during the intraday scheduling phase to maintain grid stability. Literature [23] introduces an opportunity-constrained optimization operation model to reflect the operational benefits of distributed microgrids. By calculating and balancing the economic benefits and uncertainty risks of microgrid scheduling, the operational mode of microgrids is effectively optimized. Literature [24] addresses the challenges of generation and load uncertainty posed by the integration of distributed energy into distribution grids, proposing a multi-timescale collaborative optimization scheduling framework. In addition to the day-ahead scheduling and intraday optimization scheduling models, it also establishes a real-time adjustment optimization model aimed at meeting the flexibility requirements of distribution grids at different timescales. Literature [25] also proposes a dual-timescale energy management method for distributed energy communities, using column constraint generation algorithms to optimize day-ahead scheduling strategies under uncertain conditions, while combining rolling optimization methods with short-term source-load forecasting to ensure the consistency of intraday scheduling plans and real-time supply-demand balance. Literature [26] designs a power scheduling strategy structure considering the random characteristics of renewable energy. By obtaining typical power scenarios in a virtual environment, the established power pricing and collaborative scheduling models can effectively balance economic efficiency and flexibility, achieving the maximum benefits of distributed distribution grids. Reference [27] constructs a comprehensive energy system optimization scheduling model for photovoltaic power generation with the objective of minimizing operating costs. This model transforms the source-load uncertainty problem into a mixed-integer linear programming problem, and the resulting solution range effectively enhances the local absorption capacity of distributed photovoltaic systems, thereby improving the economic efficiency of system operation. Literature [28] combines opportunity constraint methods to model the optimal scheduling of microgrid battery storage, using discrete step transformation methods to convert uncertainty modeling into an easily solvable mixed-integer linear programming form, thereby enhancing the reliability and economic efficiency of microgrid operation modes. In summary, with the rapid development of distributed photovoltaic power generation, the comprehensive scheduling model for photovoltaic systems in distribution grids can ensure high economic efficiency during operation and enhance the grid's absorption capacity for distributed energy. Therefore, considering the uncertainty characteristics of photovoltaic energy, designing a targeted energy scheduling optimization model is of great significance.

The paper first proposes an integrated strategy framework combining prediction, regulation, and decision-making. It combines the adaptive generation of confidence intervals for photovoltaic output and load electricity consumption based on Gaussian process regression (GPR) with the construction of uncertainty sets in robust optimization, establishing an adaptive robust optimization scheduling model based on interval probability uncertainty sets. The fixed term of the uncertainty set in the adaptive robust optimization scheduling model is generated using GPR, followed by adjusting the risk level considered in the decision-making phase to determine the fluctuating term within the uncertainty set, thereby defining the boundaries of the uncertainty set under different scheduling conservativeness levels. Subsequently, a large number of scenarios are obtained using the Latin hypercube sampling method, and K-means clustering is applied to reduce the number of scenarios. The effectiveness of the proposed model is validated through case study comparisons and analyses. The paper further proposes a multi-state ant colony-bacterial foraging algorithm to achieve maximum power tracking of photovoltaic systems under local shading conditions. Ant colony algorithms, fuzzy control, and perturbation observation methods are selected as reference objects. From the study of maximum power tracking under static local shading conditions, the advantages and disadvantages of the four algorithms are compared, and microgrid operation control strategies are proposed.

2 Design of an optimization model for a distributed photovoltaic dispatch system

2.1 Two-stage adaptive robust optimization scheduling strategy framework

The adaptive robust optimization scheduling strategy proposed in this paper consists of two stages: day-ahead forecasting and day-ahead scheduling. The framework of the two-stage adaptive robust optimization scheduling strategy is shown in Figure 1. Day-ahead forecasting utilizes historical data on photovoltaic power output and electricity consumption to employ GPR adaptive methods to generate the mean and variance of the predicted values for these variables, thereby establishing an uncertainty set associated with the historical data. The scheduling strategy first adjusts the risk level, then calculates the corresponding confidence level to regulate the boundaries of the uncertainty set, thereby controlling the conservatism of the robust optimization to achieve a balance between benefits and risks. The optimization scheduling model is set up in the day-ahead scheduling phase, where the day-ahead phase employs a two-stage robust optimization model, with the first and second stages corresponding to the pre-scheduling and re-scheduling phases, respectively. The pre-scheduling referred to in the proposed optimization scheduling strategy involves making partial decisions to determine the operational/charging/discharging status of controllable micro-power sources. During the re-scheduling phase, the decisions made in the pre-scheduling phase and the uncertainty parameters are finalized, based on which the output power of controllable micro-power sources and the day-ahead power purchase/sale plans with the main grid are determined.

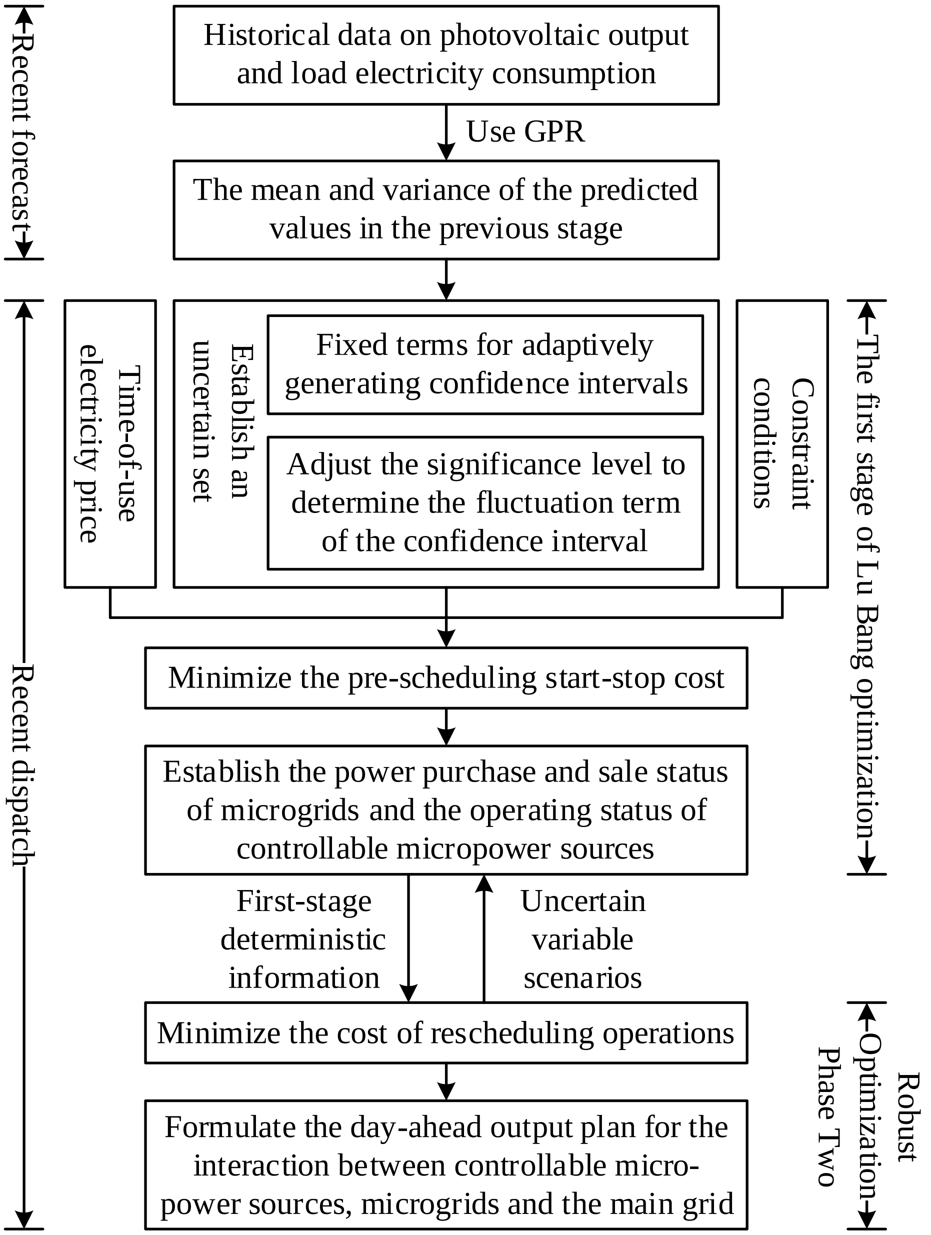

Figure 1: Two-stage adaptive robust optimization scheduling strategy framework

2.2 Adaptive robust optimization scheduling model based on interval probability uncertainty sets

The operational objective of a microgrid is to maximize overall profits while meeting operational limits. In response to the uncertainty caused by fluctuations in photovoltaic output and load consumption, this paper proposes a microgrid adaptive robust optimization dispatch model based on interval probability uncertainty sets. This model includes pre-dispatch and re-dispatch stages.

2.2.1 Day-ahead forecasting based on GPR

The process of change in the VPP bidding space is a typical time-varying, dynamic, nonlinear process that cannot be modeled using complex models based on its composition and internal parameters. Gaussian Process Regression (GPR) is a statistical learning method based on Bayesian principles, suitable for nonlinear modeling. The GPR prediction principle proposed in this paper, based on phase space reconstruction, is shown in Figure 2. First, the original data is subjected to phase space reconstruction, with its length and dimensions reconstructed to form a training set. The training set is then input into the GPR model, The model optimizes the training set to obtain the prior distribution followed by the training set data. Then, the test set is input, and the joint prior distribution followed by the test set and training set is calculated. This is converted into a posterior distribution using Bayesian principles. The mean and covariance of the distribution followed by the posterior model are used to predict the test set and output the prediction results. This approach demonstrates excellent adaptability for predicting phase space variables.

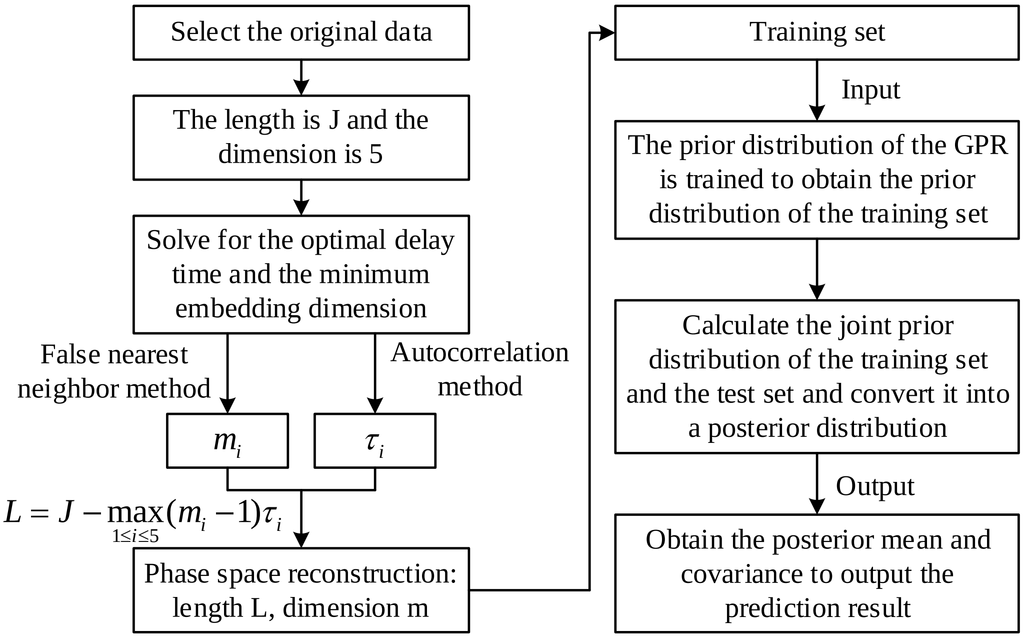

Figure 2: Schematic diagram of GPR prediction

The dimension of the time series in the training set increases from 5 dimensions to m dimensions, and the length decreases from J to L, where $m = m_1 + m_2 + m_3 + m_4 + m_5$. Let the observation data in the training set be:

$$(X, y), X = \{x_1, \cdots, x_L\}, y = \{y_1, \cdots, y_L\} \tag{1}$$

$$x_i = t, y_i = C_i^V, i = 1, \cdots, L \tag{2}$$

In the equation, t represents time. Due to sampling errors or deviations such as EVC and photovoltaic output measurement accuracy, the sample values y_i typically involve a certain degree of measurement error. Gaussian white noise can usually be added during training to represent the uncertainty error of the samples. Typically, white noise is set to follow a Gaussian distribution with a mean of 0 and a variance of σ_{noise}^2, denoted as $\varepsilon \sim GP(0, \sigma_{noise}^2)$. Then, the prior distribution of y follows a high-dimensional Gaussian distribution with a mean of 0, covariance $K(X,X)+\sigma_{noise}^2 I$ in a high-dimensional Gaussian distribution, denoted as:

$$y \sim GP(0, K(X,X)+\sigma_{noise}^2 I) \tag{3}$$

In the equation: I is the identity matrix. $K(X,X)$ is the L-order kernel matrix of the elements in the training set, calculated using the square exponential covariance function proposed below. The input data in the test set is denoted as x_*, and f_* denotes the predicted C_{VPP_i} corresponding to x_*. The joint prior distribution between y and f_* can be expressed as:

$$\begin{bmatrix} y \\ f_* \end{bmatrix} \sim GP\left(0, \begin{bmatrix} K(X,X)+\sigma_{noise}^2 I & K(X,x_*) \\ K(x_*,X) & K(x_*,x_*) \end{bmatrix}\right) \tag{4}$$

Based on the analytical properties of GPR and Bayes' theorem, under the condition that y is known, the posterior distribution of the predicted value f_* still follows a multivariate Gaussian distribution, whose expression is:

$$f_* \mid X, y, x_* \sim GP(\overline{f}_*, cov(f_*)) \tag{5}$$

In the formula: $\overline{f}_*$ is the mean value of the predicted C_{VPP_i}. $cov(f_*)$ is the variance of the predicted C_{VPP_i}, and the specific calculation method is as follows:

$$\begin{cases} \overline{f}_* = K(x_*,X)[K(X,X)+\sigma_{noise}^2 I]^{-1} y \\ \mathrm{cov}(f_*) = K(x_*,X) - K(x_*,X)\cdot[K(X,X)+\sigma_{noise}^2 I]^{-1} K(X,x_*) \end{cases} \tag{6}$$

As can be seen from equation (6), to describe the numerical characteristics of the test set and training set, it is necessary to measure the similarity between the inputs of the test set and training set, determine a similarity weight, and combine it with the known C_{VPP_i} data to characterize the closeness of input and output data across different dimensions. The similarity is measured using a covariance function. Given the infinite differentiability of the squared exponential (SE) covariance function, which makes it suitable for processing high-dimensional data, this paper selects the SE covariance function for training, expressed as:

$$K_{ij} = \sigma_f^2 \exp\left(-\sum_{b=1}^{m} \frac{(x_i - x_j)^2}{2l^2}\right), \quad i, j \in L \tag{7}$$

In the equation: σ_f^2 and l are hyperparameters in the covariance function, representing signal variance and variance scale, respectively. m is the dimension of the input time series.

The values of the hyperparameters determine the value of the SE covariance function in equation (7) and have a significant impact on the prediction results. The set of hyperparameters is defined as $\theta = \{\sigma_f^2, l, \sigma_{noise}^2\}$. This paper uses the maximum marginal likelihood function method to solve for the values of the hyperparameter set θ, selecting the hyperparameters by finding the θ that maximizes the marginal likelihood function $L(\theta)$.

First, the negative log-likelihood function $L(\theta)$ of the training set samples is established. Then, the partial derivative of $L(\theta)$ is calculated, and the optimal values of the hyperparameters θ are obtained by finding the minimum value of the partial derivative. The calculation method is as follows:

$$L(\theta) = -\frac{1}{2} y^T C^{-1} y - \frac{1}{2} \ln |C| - \frac{n}{2} \ln 2\pi \tag{8}$$

$$\frac{\partial L(\theta)}{\partial \theta} = \frac{1}{2} tr((\alpha\alpha^T - C^{-1}) \frac{\partial C}{\partial \theta}) \tag{9}$$

$$C = K(X, X) + \sigma_{noise}^2 I \tag{10}$$

$$\alpha = (K(X, X) + \sigma_{noise}^2 I)^{-1} y = C^{-1} y \tag{11}$$

In the formula, $tr(\cdot)$ is the trace operation of a matrix. Using the above method, the hyperparameters of GPR can be obtained, thereby completing the establishment of the GPR prediction model.

2.2.2 Uncertainty Set Modeling

By leveraging the probabilistic characteristics inherent in photovoltaic power generation and electricity demand, it is possible to reduce the conservatism of decision-making outcomes, establish a connection between the forecasting phase and the scheduling phase, and enhance the rationality of optimized scheduling. Given that the uncertainty of photovoltaic power output can be represented as a prediction error with a zero mean and a normal distribution, and the uncertainty of load electricity consumption can also be approximated using a normal distribution probability model, the historical values of photovoltaic power output and load electricity consumption can be considered to follow a normal population. The prediction values generated adaptively based on historical values can be regarded as samples drawn from the normal population. Therefore, this paper proposes the following new uncertainty set based on interval probability:

$$U_{in} = \begin{cases} \mu_* - z_{\alpha/2}\sigma_* / \sqrt{n} < \mu < \mu_* + \\ z_{\alpha/2}\sigma_* / \sqrt{n}, \quad \sigma_*^2 \text{Known} \\ \mu_* - t_\alpha (n-1) s / \sqrt{n} < \mu < \mu_* + \\ t_\alpha (n-1) s / \sqrt{n}, \quad \sigma_*^2 \text{Unknown} \\ 0 < \alpha < 1, 0 < n \le 30, n \in Z, \text{Small sample} \end{cases} \tag{12}$$

In the formula: μ_* is the mean of the predicted values. σ_*^2 is the variance of the predicted values. n is the sample size. $z_{\alpha/2}$ is the two-sided α percentile of the standard normal distribution, α is the significance level, and adjusting α allows scaling of the uncertainty set boundaries. $t_\alpha(n-1)$ is the two-tailed $(0 < \alpha < 1)$ percentile of the t distribution with $n-1$ degrees of freedom. s is the standard deviation of the sample. GPR is applied to historical data on photovoltaic output and load electricity consumption to obtain the mean and variance of the output prediction values for each time period within 24 hours. This uncertainty set is structurally presented as a prediction interval with probability, and its probabilistic meaning is implied in the interval between the upper and lower bounds of the new uncertainty set. This setup associates the key information contained in the historical data with the uncertainty set, thereby minimizing the loss of effective decision-making information during the prediction phase, reducing the weight and conservatism of subjective factors in the uncertainty set, and consequently reducing robust optimization modeling errors.

The accuracy of the prediction results directly impacts scheduling strategies, so it is necessary to conduct a precision analysis of the predicted values for photovoltaic output and electricity demand obtained using GPR. The Mean Absolute Error Percentage (MAE) metric is used to measure prediction accuracy, with the specific calculation formula as follows:

$$M_{AE}=\frac{\frac{1}{n}\sum_{t=1}^{24}|f_t-d_t|}{\frac{1}{n}\sum_{t=1}^{24}d_t}=\frac{\sum_{t=1}^{24}|f_t-d_t|}{\sum_{t=1}^{24}d_t} \tag{13}$$

In the formula: f_t is the predicted value. d_t is the actual value.

2.2.3 Constraints

1) Micro gas turbine (MT) start-stop constraints:

$$\begin{cases} u_{MT}^t+s_{MT}^t\le 1 \\ 0\le u_{MT}^t\le 1 \\ 0\le s_{MT}^t\le 1 \end{cases} \tag{14}$$

In the equation, u_{MT}^t and s_{MT}^t are binary variables representing the MT's on and off states, respectively. When u_{MT}^t is 1, it means that the MT is on, and when s_{MT}^t is 1, it means that the MT is off.

2) Diesel generator (DG) start-stop constraints:

$$\begin{cases} u_{DG}^t+s_{DG}^t\le 1 \\ 0\le u_{DG}^t\le 1 \\ 0\le s_{DG}^t\le 1 \end{cases} \tag{15}$$

In the equation, u_{DG}^t and s_{DG}^t are binary variables representing the DG on and off states, respectively. When u_{DG}^t is 1, it means that the DG is on, and when s_{DG}^t is 1, it means that the DG is off.

3) System power balance constraint:

$$\begin{gathered} P_{dis}(t)+P_{buy}(t)+P_{MT}(t)+P_{DG}(t) \\ +u_{PV}(t)-P_{ch}(t)-P_{sell}(t)=u_L(t) \end{gathered} \tag{16}$$

In the equation: $P_{dis}(t)$ and $P_{ch}(t)$ represent the charging and discharging power of energy storage during time interval t, respectively. $P_{buy}(t)$ and $P_{sell}(t)$ represent the power purchased and sold by the microgrid from the main grid during time interval t, respectively. $P_{MT}(t)$ represents the output power of the MT at time t. $P_{DG}(t)$ represents the output power of the DG at time t. $u_{PV}(t)$ and $u_L(t)$ represent the output power of the PV system and the load power consumption at time t, respectively.

4) MT output constraints:

$$\begin{cases} P_{MT}^{\min} \le P_{MT}(t) \le P_{MT}^{\max} \\ -R_{MT} \le P_{MT}(t) - P_{MT}(t-1) \le R_{MT} \end{cases} \tag{17}$$

In the formula: $P_{MT}^{\min}$ and $P_{MT}^{\max}$ are the minimum and maximum output power of MT, respectively. R_{MT} is the maximum climbing power of MT.

5) DG output constraint:

$$\begin{cases} P^{DG,min} \le P_{DG}(t) \le P^{DG,max} \\ P_{DG}(t) - P_{DG}(t-1) \le P^{DG,up} \end{cases} \tag{18}$$

In the formula: $P^{DG,\min}$ and $P^{DG,\max}$ are the upper and lower limits of DG output power, respectively. P^{DGup} is the maximum ramp rate of DG.

6) Energy storage operation constraints:

$$\begin{cases} 0 \le P_{dis}(t) \le U_S(t) P_S^{\max} \\ 0 \le P_{ch}(t) \le [1 - U_S(t)] P_S^{\max} \\ B_S^{\min} \le B_{St} \le B_S^{\max} \\ S_{OCt} = S_{OC(t-1)} - P_{ch}(t)\eta^c / E \\ S_{OCt} = S_{OC(t-1)} - P_{dis}(t) / E\eta^d \\ S_{OC}^{\min} \le S_{OCt} \le S_{OC}^{\max} \end{cases} \tag{19}$$

In the equation: $P_{dis}(t), P_{ch}(t)$ represent the charging and discharging power of the energy storage system at time t, respectively. $U_S(t)$ represents the charging and discharging status of the energy storage system, with values of 0 and 1 representing charging and discharging, respectively. $P_s^{\max}$ is the maximum allowable charging and discharging power of the energy storage system. $B_s^{\max}$ and $B_s^{\min}$ are the maximum and minimum remaining capacities allowed for the energy storage system during the scheduling process. B_{St} is the remaining capacity of the energy storage system at time t. S_{OCt} is the state of charge of the energy storage system at time t. $S_{OC(t-1)}$ is the state of charge of the energy storage system at time $t-1$, and $S_{oc}^{\min}$ and $S_{oc}^{\max}$ are the minimum and maximum values of the state of charge of the energy storage system, respectively. η^c and η^d are the charging and discharging efficiencies of the energy storage system, respectively. E is the capacity of the energy storage device. To promote the recycling of energy storage, within the scheduling period N_T (24 hours), the capacity of the energy storage device is equal at the beginning and end of the scheduling period, i.e., $\eta^c \sum_{t=1}^{N_T}[P_{ch}(t)\Delta t_c] = (1/\eta^d)\cdot\sum_{t=1}^{N_T}[P_{dis}(t)\Delta t_d]$ ($\Delta t_c, \Delta t_d$ represent the charging and discharging durations of energy storage, respectively).

7) Power exchange constraints between the microgrid and the main grid:

$$\begin{cases} 0 \le P_{buy}(t) \le U_M(t)P_{grid,\max} \\ 0 \le P_{sell}(t) \le [1-U_M(t)]P_{grid,\max} \end{cases} \tag{20}$$

In the equation: $P_{grid,\max}$ is the power limit for interaction between the microgrid and the main grid. $U_M(t)$ is the power purchase and sale status between the microgrid and the main grid. A value of 1 indicates that the microgrid is purchasing power from the main grid, while a value of 0 indicates that the microgrid is selling power to the main grid.

2.2.4 Adaptive Robust Optimization Scheduling Model

In order to further reduce the conservatism of decision-making results and enhance the adaptability of the model, the following two-stage optimization scheduling model is designed:

$$\begin{cases} \min_x\{C_{one} + \max_{u\in U} \min_{y\in F(x,u)} C_{two}\} \\ s.t. C_{one} = C^T x, C_{two} = D^T y \end{cases} \tag{21}$$

In the equation: C_{one} is the objective function for the first stage, i.e., the pre-dispatch cost for the day-ahead stage. C_{two} is the objective function for the second stage, i.e., the re-dispatch cost for the day-ahead stage. $C^T x$ is the sum of the startup/shutdown costs of MT and DG. $D^T y$ is the sum of other costs in the day-ahead scheduling cost excluding the startup/shutdown costs of MT and DG

U is the uncertainty set, including the uncertainty of PV output and load electricity consumption. u is the uncertainty variable, including the PV output and load electricity consumption power in the microgrid. x and y are the decision variable vectors for the pre-scheduling and re-scheduling stages, respectively, where $U_M(t) \in x$, $P_{buy,t}$, and $P_{sell,t} \in \gamma$. $P_{buy,t}$ is the electricity purchased by the microgrid from the main grid during time period t. $P_{sell,t}$ represents the electricity sold by the microgrid to the main grid during time period t. $F(x,u)$ denotes the feasible region formed by the decision variables x and the uncertain variable u in the pre-dispatch phase, with the specific expression as follows:

$$F(x,u) = \begin{Bmatrix} y\,| & \\ Dy \ge d, & \rightarrow \gamma \\ Ky = k, & \rightarrow \lambda \\ Ex + Gy \ge h, & \rightarrow v \\ I_u y = u & \rightarrow \pi \end{Bmatrix} \tag{22}$$

In the equation, γ, λ, v, π represent the dual variables corresponding to each constraint in the minimization problem of the rescheduling stage.

The first stage is the pre-scheduling stage. In this stage, the operating states of MT and DG are determined so that the microgrid system can cope with various photovoltaic output and load scenarios. The pre-scheduling objective function is

$$\begin{cases} \min C_{one} = C_{MT}^{on} + C_{MT}^{off} + C_{DG}^{on} + C_{DG}^{off} \\ C_{MT}^{on} = C_u \sum_{t=1}^{N_T} u_{MT}^t \\ C_{MT}^{off} = C_d \sum_{t=1}^{N_T} s_{MT}^t \\ C_{DG}^{on} = c_{on} \sum_{t=1}^{N_T} u_{DG}^t \\ C_{DG}^{off} = c_{off} \sum_{t=1}^{N_T} s_{DG}^t \end{cases} \tag{23}$$

In the equation: $C_{MT}^{on}, C_{MT}^{off}$ represent the startup and shutdown costs of MT during the scheduling period, respectively. $C_{DG}^{on}, C_{DG}^{off}$ represent the startup and shutdown costs of DG within the scheduling cycle, respectively. c_u, c_d are the unit startup/shutdown costs of MT, respectively. c_{on}, c_{off} are the unit startup/shutdown costs of DG, respectively. u_{MT}^t, u_{DG}^t are binary variables representing the startup status of MT and DG, respectively, with a value of 1 indicating startup. s_{MT}^t, s_{DG}^t are binary variables representing the shutdown status of MT and DG, respectively, with a value of 1 indicating shutdown.

The second stage is the rescheduling stage. Based on the results obtained from the pre-scheduling stage, rescheduling is performed using GPR to obtain the day-ahead forecast values for PV output and load electricity consumption. Under the condition that the operational status of controllable micro-power sources is determined, deterministic optimization methods are used to calculate the equipment output and the microgrid's electricity purchase and sale quantities, ensuring the operational reliability of the microgrid. The rescheduling objective function is:

$$\max_{u \in U} \min_{y \in F(x,u)} C_{two} = D_{MT} + D_{DG} + D_{BS} + D_{grid} \tag{24}$$

$$s.t. D_{MT} = \sum (a_{MT} P_{MT}(t) + c_{MT}) \Delta t \tag{25}$$

$$D_{DG} = \sum u^t [b_i P_{DG}^2(t) + d_i P_{DG}(t) + e_i] \tag{26}$$

$$D_{BS} = \sum B_{BS,t}^j (P_{c,t}^j \eta^c + \frac{P_{d,t}^j}{\eta^d}) \tag{27}$$

$$D_{grid} = \sum_{t \in N_T} (C_{buy,t} P_{buy,t} - C_{sell,t} P_{sell,t}) \tag{28}$$

In the equation: $D_{MT}, D_{DG}, D_{BS}, D_{grid}$ represent the operating costs of MT, DG, energy storage charging and discharging, and microgrid power purchase and sale, respectively. a_{MT}, c_{MT} are the operating cost coefficients for MT. $P_{MT}(t)$ is the output power of MT during the t time period. Δt is the scheduling duration. b_i, d_i, e_i are the fuel cost coefficients for diesel generators. $P_{DG}(t)$ is the output power of DG at time t. $B_{BS,t}^{j}$ is the operating cost coefficient of the j th energy storage system during the t time period. $P_{c,t}^{j}$ and $P_{d,t}^{j}$ are the charging and discharging power of the j th energy storage system during the t time period, respectively. η^c and η^d are the charging and discharging efficiencies of the energy storage system, respectively. $C_{buy,t}$ is the unit price of electricity purchased by the microgrid from the main grid during time period t. $C_{sel,t}$ is the unit price of electricity sold by the microgrid to the main grid during time period t.

2.3 Case Study Analysis

This paper establishes an adaptive robust optimization scheduling model based on interval probability uncertainty sets. Typical summer wind power, photovoltaic, and load data from a city in Northwest China are selected to validate the feasibility of the model, which is solved using MATLAB and its Ceplex toolbox. This paper compares the deterministic model (Model 1), the classical two-stage robust optimization model (Model 2), and the model proposed in this paper (Model 3). In Model 2, the prediction error for wind power and photovoltaic power output fluctuations is 12%, and the prediction error for load power fluctuations is 8%.

2.3.1 Evaluation based on LHS wind, solar, and load uncertainty sets

Since wind power, photovoltaic power output, and load power follow Weibull, beta, and normal distribution functions, respectively, this paper uses the Latin hypercube sampling method to sample 1,000 scenarios from their corresponding probability distribution functions. To reduce computational complexity, the Euclidean distance between each scenario is calculated using the k-means clustering method, and scenarios without characteristics are removed, reducing the number of scenarios to 10. Finally, the calculated probabilities were used as weights for weighted processing to obtain the output ranges for wind power, solar power generation, and load demand. The output power fluctuation intervals for wind power, photovoltaic power, and load power are shown in Figure 3 (Figure a represents the uncertainty set of wind power and photovoltaic output power, with the solid line indicating the day-ahead forecast power. The lines a to f in the figure represent the upper bound of the photovoltaic interval, the lower bound of the photovoltaic interval, the day-ahead photovoltaic output power, the upper bound of the wind power interval, the lower bound of the wind power interval, and the day-ahead wind power output, respectively. Figure b shows the uncertainty set for load power, where lines a–c represent the upper bound of the load interval, the lower bound of the load interval, and the load power for the previous day, respectively.

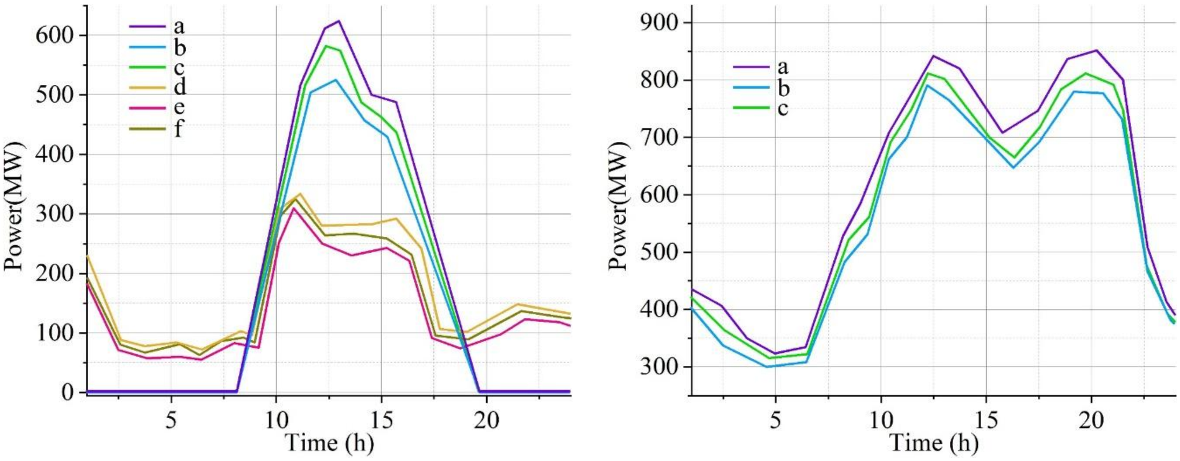

(a) Fluctuation range of wind and photovoltaic power

(b) Fluctuation range of load power

Figure 3: Fluctuation ranges of wind, photovoltaic power and load power

2.3.2 Comparison of operating costs for different optimization models

The comparison of operating costs for different models is shown in Table 1. As can be seen from the table, the total operating cost of Model 3 is 309,600 yuan lower than that of Model 2, primarily due to differences in the selection of prediction intervals. Model 2 is a traditional robust optimization model, where the output intervals for wind power and photovoltaic power are set to ±15% of the previous day's predicted power, and the load demand is set to ±10% of the previous day's predicted power. Model 3, on the other hand, uses LHS to re-estimate the prediction intervals. The intervals obtained through this method are slightly smaller than those of Model 2, effectively reducing conservatism. The wind, solar, and load output power based on Model 3 are shown in Figure 4 (Figure a shows the output distribution of wind power and photovoltaic power, where the lines a–f represent the upper bound of the photovoltaic interval, the lower bound of the photovoltaic interval, the photovoltaic output scenario, the upper bound of the wind power interval, the lower bound of the wind power interval, and the wind power output scenario, respectively. Figure b shows the load power demand distribution, where a–c represent the upper bound of the load interval, the lower bound of the load interval, and the load power scenario, respectively. The uncertainty is concentrated during peak load periods, with wind power and PV output taking the lower bound values concentrated between the 10th and 18th hours, and load taking the upper bound of the interval concentrated between the 10th and 22nd hours. Compared to Model 1, which uses expected output conditions, Model 3 has each unit bear an additional load of approximately 82 MW during peak electricity consumption periods. This load is balanced through energy storage station discharge and reduction of transferable load, resulting in significantly higher thermal power operation costs and transferable load compensation costs for Model 3 compared to Model 1.

Table 1: Operating costs of different models

Cost(10^4CNY)	Model 1	Model 2	Model 3
The operating cost of the fire crew	185.66	232.54	201.32
Outage cost	10.78	10.78	10.78
Energy storage power plant from discharge cost	7.85	7.97	7.96
Translation load compensation cost	0.28	0.78	1.05
Total cost	204.57	252.07	221.11

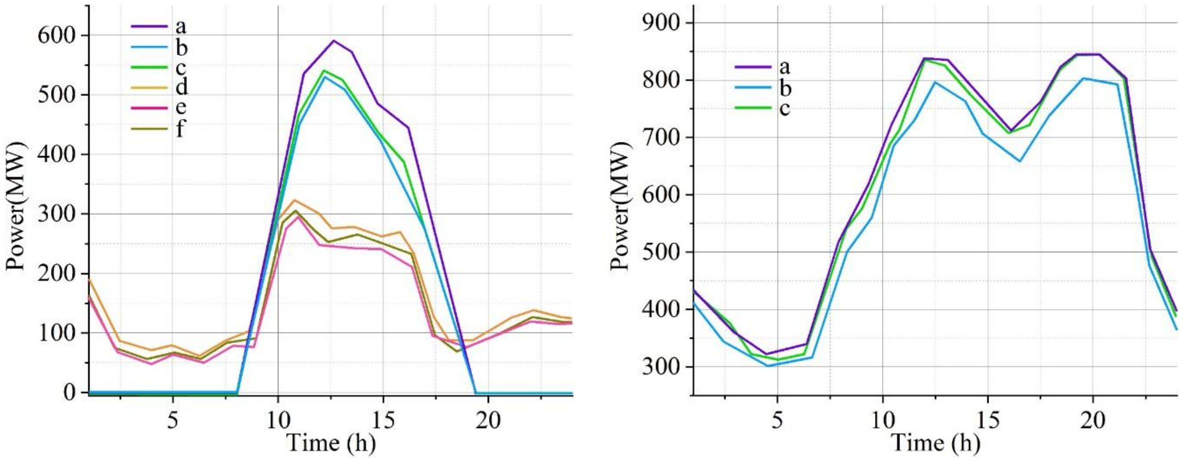

(a) Output distribution of wind and photovoltaic power

(b) Output distribution of load power

Figure 4: Output power of wind, photovoltaic and load power based on Model 3

2.3.3 Output Analysis of Thermal Power Units and Energy Storage Power Stations

The power output distribution of the power generation units derived from Model 3 is shown in Figure 5. During the 0–8 a.m. time period, the load exhibits an upward trend, with relatively low wind power output. The system primarily relies on thermal power generation units and energy storage systems to maintain power balance. During the 9–18 hour period, the load continues to rise, while wind and solar power output gradually increases. To promote the consumption of wind and solar power, the output of thermal power plants is reduced as much as possible, and the energy storage system is charged when necessary. During the 19–22h period, wind and solar power output decreases. Since the ramp-up speed of thermal power plant output is slower than the decrease in wind and solar power generation, the energy storage system must discharge to maintain power balance during this period. After 22:00, as load demand decreases, the output of thermal power units is also constrained by ramping limitations. The reduction rate of thermal power unit output is slower than the decline in load demand, so charging the energy storage system can be prioritized.

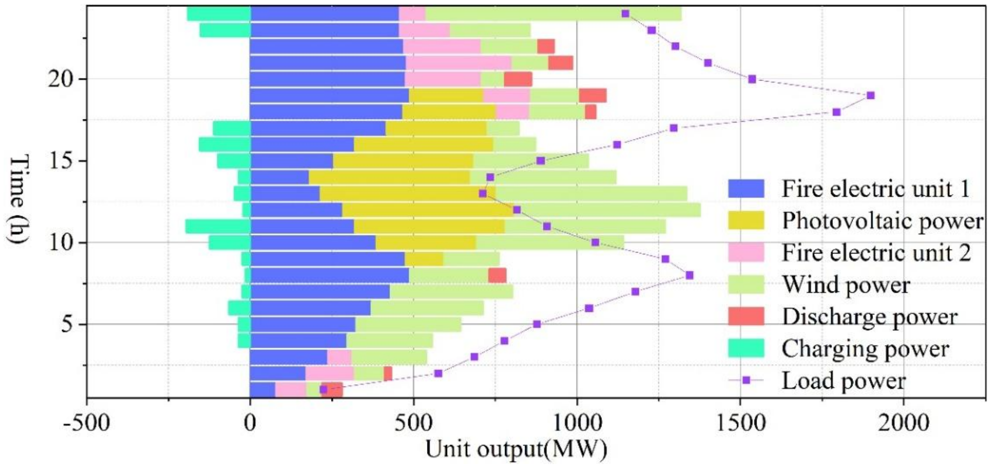

Figure 5: The output distribution of the unit obtained from Model 3

The transfer of shiftable loads in Models 2 and 3 is shown in Figure 6. During the 13–22 h time period, the peak-to-valley difference is 105 MW. The peak-to-valley differences for shiftable loads in Models 2 and 3 are 69.32 MW and 49.14 MW, respectively. As shown in the table, the cost of compensating for the shiftable load in the latter model is 0.27 million yuan higher than in the former model. However, the peak-to-valley difference in Model 3 is smaller than that in Model 2, and the slope of the load curve is more gradual, indicating that the shiftable load in this model has stronger mobility. The proposed model demonstrates superior peak-shaving and valley-filling capabilities compared to traditional models, effectively reducing the difficulty of peak regulation in the system.

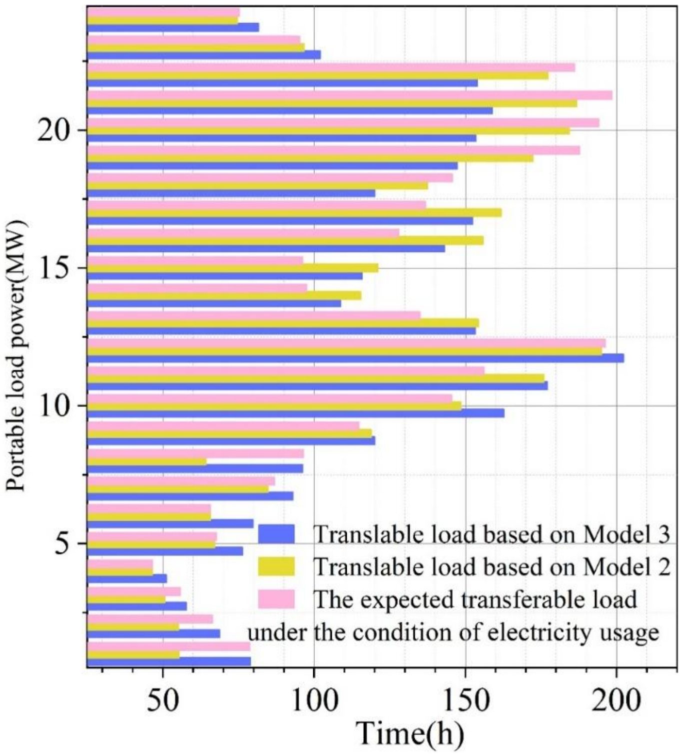

Figure 6: Shiftable load of Model 2 and Model 3

3 Microgrid operation control strategy based on photovoltaic maximum power point tracking

3.1 Research on photovoltaic maximum power point tracking control

In engineering applications, given the high cost of photovoltaic power generation equipment, improving the conversion efficiency of solar energy to electricity while ensuring the safe and stable operation of the system holds significant practical value. Therefore, this chapter focuses on maximum power point tracking (MPPT) of photovoltaic arrays as the research object for photovoltaic-storage direct current microgrids. By controlling the duty cycle of the switching elements in the photovoltaic system's converter, maximum power tracking technology enables the photovoltaic array to output maximum power to the external circuit even under varying environmental conditions. Photovoltaic cells exhibit highly nonlinear functional relationships, and their voltage-current and voltage-power output curves vary under uneven sunlight and temperature changes, causing the maximum power point to shift. Additionally, due to natural factors such as clouds, dust layers, and buildings, photovoltaic (PV) arrays are exposed to varying light intensities and temperature deviations, i.e., partial shading conditions (PSC). Under such conditions, the PV voltage-power curve exhibits multiple local maximum power points, resulting in a multi-peak characteristic. Conventional MPPT techniques such as disturbance observation method, conductance increment method, and hill-climbing method are prone to getting stuck at local maximum power points, leading to high power losses in the PV system. Therefore, MPPT under PSC conditions is crucial for maintaining the efficient operation of the PV system. Currently, bio-inspired algorithms based on biological behavior exhibit good reliability, robustness, and flexibility, making them the most popular algorithms for seeking the maximum power point under PSC. This section proposes a multi-state ant colony-bacterial foraging algorithm (PACO-BFOA) to achieve maximum power output for PV systems under partial shading conditions. Simulation results demonstrate that the proposed algorithm can rapidly and stably online locate the global maximum power point under both partial shading and varying light conditions.

3.1.1 Polymorphic Ant Colony-Bacterial Foraging Algorithm (PACO-BFOA)

PACO-BFOA introduces an information diffusion mechanism based on the ACO principle to enable more thorough information transmission between ant colonies, simulates polymorphic ant colonies to balance local and global performance, and uses bacterial chemotaxis behavior to guide the local exploration of ants, further improving the algorithm's convergence stability and optimization capabilities [29]. The PACO-BFOA algorithm implementation is shown in Figure 7.

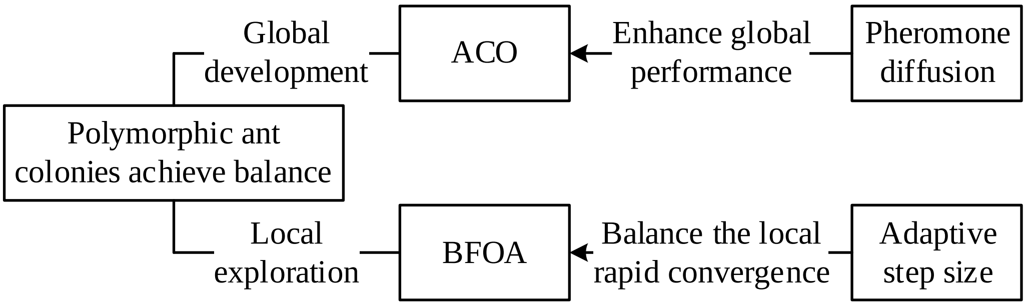

Figure 7: Implementation of the PACO-BFOA algorithm

(1) Pheromone diffusion mechanism

(a) Pheromone diffusion principle

There are two paths from c to f, cdef and cbaf. Suppose that the initial information quantities of cd and cb are the same. Since cd is shorter than cb, M is more likely to move to d in the next step. If an ant M_1 has previously moved from b to a (the distance between b and a is very short), the pheromone secreted by M_1 will diffuse. When the pheromone concentration on cb reaches a certain level, M is more likely to choose b as the next destination compared to the pheromone concentration on cd. It can be seen that the pheromone diffusion mechanism can effectively reduce optimization interference.

(b) Pheromone Diffusion Model

After incorporating the pheromone diffusion mechanism into ACO, the concentration of information diffusion in space roughly follows a Gaussian distribution in relation to distance. The farther the distance from the source, the lower the concentration of diffused pheromones. The diffusion model for a single ant is shown in Equation (29):

$$f(x) = a \cdot e^{-\frac{(x-b)^2}{2c^2}} \tag{29}$$

In the equation: x represents the distance from the source. a denotes the amount of information secreted by the source. b denotes the position of the source. c is the standard deviation, which characterizes the diffusion ability of the information.

Suppose that the initial information quantity of the source b is a_1, and M produces an information quantity of size a_2 after passing through b. The information quantity of all paths is denoted by y. Then, after M passes through b, the information quantities on all relevant paths are shown in equations (30) to (32).

$$y_{k+1} = y_k - \rho \cdot f_1 + \rho \cdot f_2 \tag{30}$$

$$f_1 = a_1 \cdot e^{-\frac{(x-b)^2}{2c_1^2}} \tag{31}$$

$$f_2 = a_2 \cdot e^{-\frac{(x-b)^2}{2c_2^2}} \tag{32}$$

In the equation: y_k represents the amount of information on all paths after the k th ant moves. y_{k+1} represents the amount of information on all paths after the $k+1$ th ant moves. ρ represents the pheromone evaporation coefficient, with a value range of $\rho \in [0,1]$.

(2) Multimodal Ant Colony

Ant colony systems are often complex and orderly, with ants collaborating and dividing labor among themselves. However, traditional single-ant colony algorithms do not consider the differences in ant behavior, ignoring the complexity of ant colony systems. Having all ants perform the same task fails to maximize the collaborative capabilities of the ant colony system. Areas with high information density are more likely to yield optimal solutions, so scout ants that produce more pheromones primarily perform local scouting through chemotaxis. Search ants, which produce fewer pheromones, primarily handle global exploration. Therefore, PACO-BFOA primarily uses scout ants and search ants to balance local exploration and global development.

(3) Bacterial foraging for local exploration

Chemotaxis enables bacteria to have good local exploration capabilities, including rolling and swimming. When the pheromone concentration at the current point is less than the state transition factor P_0, the ant simulates bacteria swimming in any direction $\phi(j)$, defined as the forward direction after rolling. Swimming evaluates the direction of rolling; if the fitness value improves after rolling, the original rolling direction is maintained; otherwise, rolling is performed again. Ant chemotaxis is shown in the equation.

$$\theta(j+1) = \theta(j) + S(j)\phi(j) \tag{33}$$

$$\phi(j) = \frac{\lambda_j}{\sqrt{\lambda_j^T \lambda_j}} \tag{34}$$

In the equation: j represents the number of chemotaxis steps. θ is the position of the ant. $S(j)$ is the walking stride length. λ_j is the walking direction.

To ensure that the algorithm has a high search speed in the early stages of the search, better convergence performance in the later stages of the search, and to avoid oscillation, this paper uses an adaptive step size to balance the speed and convergence of local search, as shown in Equation (35).

$$S(j) = S_{\max}\left(\frac{I-j}{I}\right)^2 \tag{35}$$

In the formula: $S_{\max}$ is the initial step size. I is the maximum number of iterations.

3.1.2 Photovoltaic MPPT Design of PACO-BFOA

To achieve maximum power tracking output for the photovoltaic system, the power of the PV system, P_{PV}, is used as the fitness function. Under fixed external conditions, the output power of the PV system is mainly determined by the voltage. Therefore, the objective function of the photovoltaic system is:

$$P_{PV} = I_{PV}(V_{PV}) \cdot V_{PV}(T,G) \tag{36}$$

In the equation: V_{PV} represents the output voltage of the photovoltaic panel. I_{PV} is the output current of the panel. T is the panel temperature. G represents the irradiance of the panel.

The structure of the photovoltaic system MPPT implemented using PACO-BFOA under PSC is shown in Figure 8. The PACO-BFOA power tracker inputs the photovoltaic panel voltage and outputs a duty cycle command, which is converted into a switching signal by the pulse width modulation (PWM) module to control the on/off state of the insulated gate bipolar transistor (IGBT), enabling the system to operate at the maximum power point.

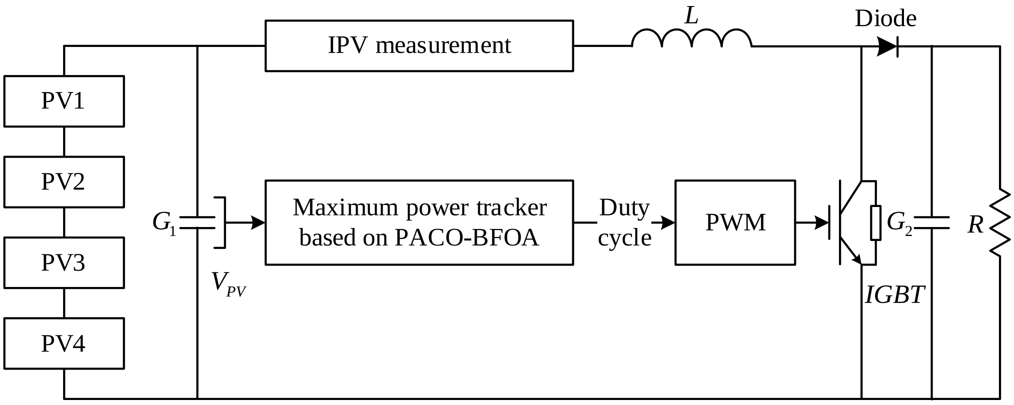

Figure 8: PACO-BFOA achieves MPPT in photovoltaic systems

The MPPT process of the photovoltaic system under PSC using PACO-BFOA is shown in Figure 9. i is the current iteration number. I is the maximum iteration number of the algorithm [30]. P_0 is the state transition factor. In order to improve the search speed of the algorithm, it is necessary to have a more comprehensive understanding of the pheromone distribution. Therefore, the ant colony is uniformly initialized within the feasible domain:

$$x_k^0 = D_{PV}^{\min} + \frac{k}{K}(D_{PV}^{\max} - D_{PV}^{\min}) \tag{37}$$

In the formula: x_k^0 is the initial position of the k th ant. $D_{PV}^{\min}$ and $D_{PV}^{\max}$ are the lower and upper limits of the duty cycle, respectively. K is the total number of ants.

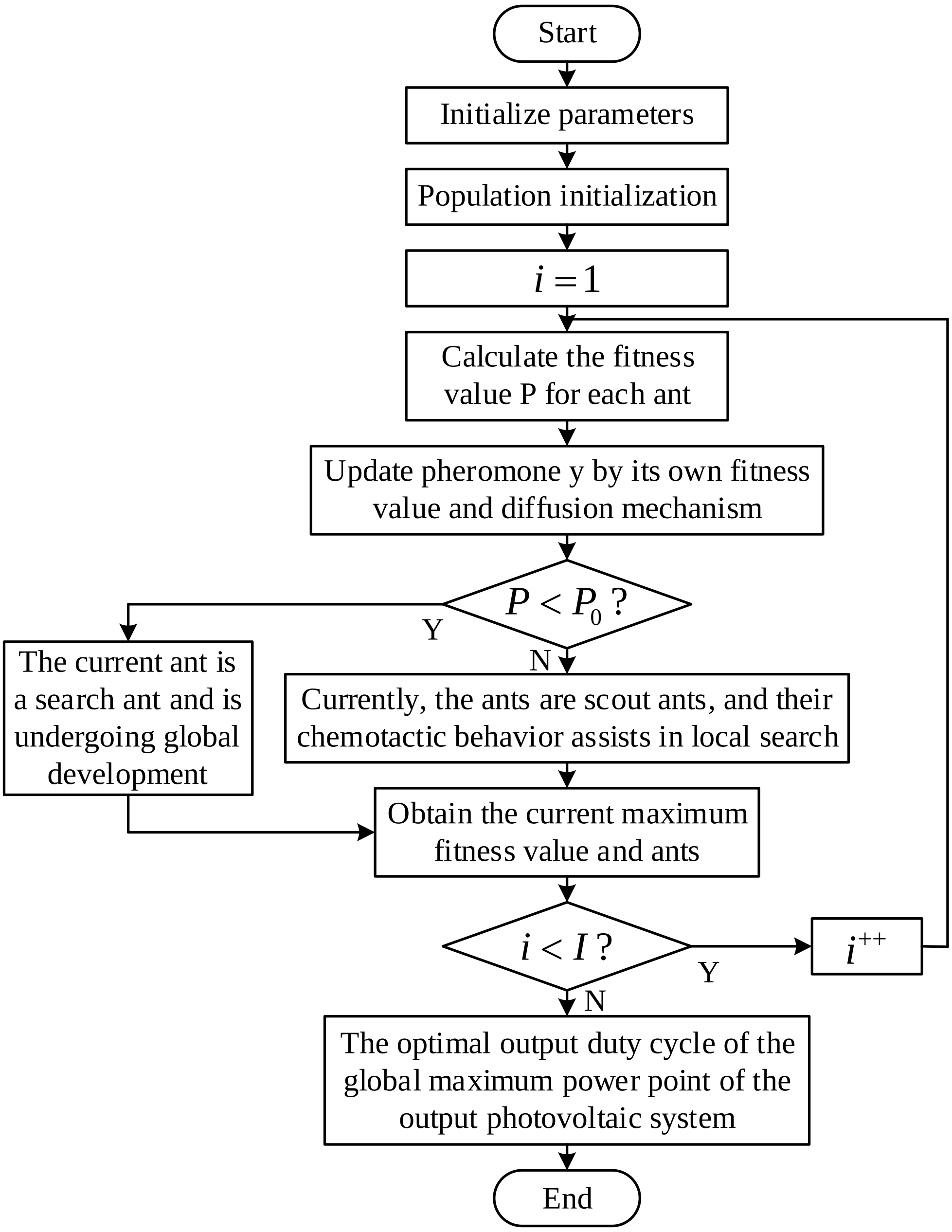

Figure 9: Implement the PACO-BFOA algorithm process for photovoltaic system MPPT

3.1.3 Analysis of results under various local shadow conditions

To verify the convergence of the PACO-BFOA algorithm in actual applications for maximum power tracking, four types of local shading distributions in photovoltaic arrays were designed for verification. The P-U characteristic curves of the photovoltaic array output under the four conditions are shown in Figure 10.

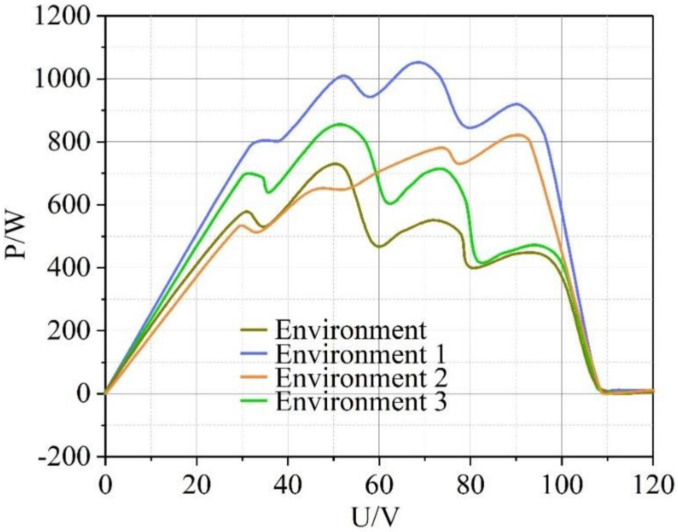

Figure 10: Four environmental output characteristic curves

The maximum power tracking output characteristics of the algorithm under four different environments are shown in Figure 11. As can be seen from Figures 10 and 11, the maximum power value tracked by the algorithm under the environment is 732.6W, with an error of only 0.01W compared to the actual maximum power. Under Environment 1, the maximum power value tracked is 1065W, with an error of only 0.4W compared to the actual maximum power. In Environment 2, the maximum power value tracked is 842.5W, with an error of only 1.36W compared to the actual maximum power. In Environment 3, the maximum power value tracked is 851.9W, with an error of only 0.25W compared to the actual maximum power. This demonstrates the convergence of the algorithm in global maximum power tracking.

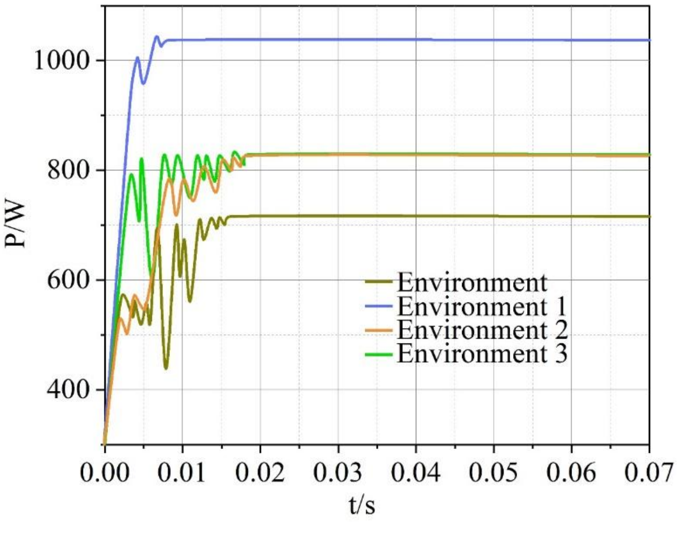

Figure 11: Maximum power tracking output characteristics in four environments

3.1.4 Analysis of the results of the polymorphic ant colony-bacterial foraging algorithm

The application effects of different algorithms in MPPT are shown in Tables 2 and 3, respectively. The algorithm designed in this paper has excellent tracking performance compared to the classic algorithm, traditional ant colony algorithm, and traditional fuzzy control in the application of maximum power point tracking in photovoltaic power generation systems. Not only has the speed of maximum power tracking been greatly improved, but the stability of the system has also been enhanced. When faced with changes in the external environment, it also exhibits very fast and stable tracking performance.

Table 2: A comparison of the outputs of four algorithms in a static state environment

Algorithm name	Maximum power output(W)	The maximum shock after stability(W)	Track time(s)
Disturbance observation method	428.1	109.8	0.5
Fuzzy control	575.5	3	0.006
Ant colony algorithm	730.73	89.4	0.003
Ours	728.4	0	0.012

Table 3: Output comparison of four algorithms in a dynamic state environment

Algorithm name	Output before 0.4s	Before before 0.4s	Percentage reduction(%)	The biggest shock after 0.4s	Track time(s)
Disturbance observation method	432.5	425.2	0.35	111	0.016
Fuzzy control	578.6	547.6	5.5	0	0.002
Ant colony algorithm	729.13	706.1	2.5	70.6	/
Ours	727.5	708.4	2.9	0.2	/

3.2 Microgrid operation control strategy

3.2.1 PQ Control Principles

In grid-connected mode, the power grid determines the operating frequency of the microgrid system. At this time, the distributed power generation (DG) sources within the microgrid (MG) output the corresponding reactive power Q and active power P. Distributed power generation sources such as photovoltaic and wind power generation, whose output power is highly influenced by external environmental factors, do not have a constant output power. Control should ensure that the output power of photovoltaic and wind power generation is maximized, for which the PO control strategy is generally adopted.

In the three-phase stationary abc coordinate system, the three-phase voltages are coupled, but in the rotating dq coordinate system, there is no coupling relationship, and u_q is zero, while u_d is a constant. Let the measured current be transformed into the d-axis current i_d and the q-axis current i_q via dq transformation. When the inverter requires active power P_{ref} and reactive power Q_{ref}, the reference values of the inverter output currents in the dq coordinate system are:

$$i_d^* = \frac{P_{ref}}{u_d} \tag{38}$$

$$i_q^* = -\frac{Q_{ref}}{u_d} \tag{39}$$

As can be seen from the formula, controlling the output power only requires controlling the output current. In other words, as long as the inverter can control the reference currents i_d^*, i_q^*, it can control the output power P and Q, thereby achieving decoupled control of active and reactive power for three-phase inverters connected to the grid.

$$P = u_d i_d + u_q i_q \tag{40}$$

$$Q = u_q i_d - u_d i_q \tag{41}$$

where u_q, u_d are the dq-axis components of the inverter-side voltage. i_q, i_d are the dq-axis components of the inverter output current.

Taking a photovoltaic power generation system controlled using the P-Q method as an example, the inverter output current, voltage, and frequency are first measured. The inverter output voltage frequency is synchronized with the bus voltage frequency via a phase-locked loop (PLL) control. The detected power values P, Q are subtracted from the active power P_{ref} and reactive power Q_{ref} (typically set to 0) at the maximum power point that the photovoltaic power generation system can generate, yielding AP, AQ. The power difference signals AP, AQ are processed through the control system to obtain i_d^*, i_q^*. These values are used as the direct-axis and transverse-axis components for the control loop. The i_d^*, i_q^* with the actual d-axis and q-axis components of the current i_d, i_q through current decoupling control, the obtained u_d, u_q are converted by the dq0/abc converter to obtain the PWM-modulated input voltage u_{abc}. The phase-locked loop is used to ensure that the output voltage of the grid-connected inverter is synchronized with the system voltage. The sin-cos signal of the system voltage is accurately acquired, where the active and reactive power outputs of the DG must satisfy the conditions $0 \le P \le P_n$ and $0 \le Q \le Q_n$.

3.2.2 Sag Control Principle

When a system failure or other reasons cause the microgrid system to disconnect from the main grid, i.e., when the microgrid system switches from grid-connected operation mode to island operation mode, the island microgrid has different characteristics and control requirements compared to the traditional grid. The main control requirements are that distributed power sources must be able to provide voltage and frequency support to the microgrid and have regulation capabilities. The aforementioned issue is one of the key aspects of the grid-connected inverter control technology for distributed power sources.

In a traditional power grid, the relationship between reactive power, active power, voltage, and frequency is as follows, where the voltage on the inverter output side is $E_l \angle \theta$, the voltage on the grid side is $E_2 \angle \theta$, and the line impedance is $Z_i = R + jX$. The power injected from point A to point B is $S = P + jQ$.

$$P = \frac{E_1[R(E_1 - E_2\cos\theta) + E_2 X \sin\theta]}{R^2 + X^2} \tag{42}$$

$$Q = \frac{E_1[X(E_1 - E_2\cos\theta) + E_2 R \sin\theta]}{R^2 + X^2} \tag{43}$$

Since the phase angle difference between the generator and the system voltage is small, i.e., $cos\theta \approx 1$. At this time, the line is inductive, i.e., $X >> R$. Neglecting R simplifies the formula, and the active and reactive output power of the generator can be approximated by the following equation:

$$P = (E_1 E_2 / X)\sin\theta \tag{44}$$

$$Q = E_1(E_1 - E_2)X \tag{45}$$

where E_1, E_2, X, θ represents the output voltage amplitude of the generator, the voltage amplitude of the PCC point, the equivalent impedance value of the access line, and the phase angle of the output voltage of the generator. As can be obtained from the above formula, the active power P of the generator output is mainly determined by the phase angle of the output voltage θ (frequency f is usually replaced by θ in practical applications), and the reactive power output power Q is mainly controlled by the voltage amplitude E_l and PQ is decoupled. From the perspective of the active power distribution between each unit and the frequency modulation needs of the system, the active power output can be adjusted in real time according to the system frequency change for the generator with adjustment ability (its output characteristic is a droop curve).

When the load changes, if the DG output power does not change accordingly, it will lead to an imbalance between the output power and the input power, resulting in significant voltage fluctuations in the system. However, when the load changes, the DG output power is coordinated and controlled accordingly, ensuring that the output power and input power are balanced. At this point, the DG output can suppress the voltage fluctuations caused by load switching in the system. In power systems, synchronous motors, due to their droop characteristics, can adjust their power output to achieve power distribution objectives by detecting their own output power, voltage, and frequency without the need for communication lines. The P-f and O-V droop control proposed in microgrids is one continuation of the aforementioned approach in traditional power systems. Its essence lies in each DG detecting the magnitude of its own line output power, approximating power decoupling to obtain the required output frequency and amplitude. From a control perspective, changes in active power P and reactive power Q influence changes in frequency f and voltage V. Based on the P-f and Q-V droop control principles, the following relationships exist between f, V and P, Q in distributed power sources:

$$f = f^* - m(P - P^*) \tag{46}$$

$$V = V^* - n(Q - Q^*) \tag{47}$$

Among these, f^* is the rated frequency, typically set to 50 Hz. f is the measured frequency of the microgrid system. m is the active power droop coefficient. V is the voltage amplitude at the inverter grid connection point. V^* is the rated voltage amplitude in grid-connected mode. n is the reactive droop coefficient. P^*, Q^* are the specified rated active and reactive power in grid-connected mode, respectively.

Two distributed power sources use droop control. When distributed power source 1 and distributed power source 2 operate at the rated frequency $f^* = 50$ Hz, their rated active power outputs are $P_{nefl}, P_{ref2}, Q_{\max i}$ is the maximum reactive power output of distributed power source i, and $V_{\min i}$ is the minimum voltage drop of distributed power source i. Since distributed power sources with different characteristics generally have different output characteristics, the ω_0 and V_0 values of the droop characteristic curves for different DGs must be the same to ensure that no circulating currents are generated between different DGs in the microgrid during no-load operation.

$$\begin{cases} m_{pi} = \dfrac{\Delta f^* 2\pi}{P_{refi}} = \dfrac{(f_0 - f^*) * 2\pi}{P_{refi}} = \dfrac{\omega_0 - \omega^*}{P_{refi}} \\ n_{qi} = \dfrac{V_n - V_{\min i}}{Q_{\max i}} \end{cases} \quad (i = 1, 2 \ldots) \tag{48}$$

Distributed power sources need to go through a grid-connected inverter to invert DC to AC. The inverter grid-side voltages V_{abc} and I_{abc} are collected by the sensor. In the power calculation module, V_{abc} and I_{abc} are transformed by dq to obtain the instantaneous active power P and reactive power Q of DG output according to the formula, and the average power of the output is obtained by the low-pass filter. The rated voltage and frequency of PCC point are $U^*, f^*, P-f, Q-V$ droop control is compared with P^* and P, and the deviation of ΔP is proportionally adjusted to obtain the frequency adjustment signal. Q^* is compared with Q, and the deviation ΔQ is proportionally adjusted to obtain the voltage peak regulation signal, and the obtained regulation signal is added to its corresponding given, and the pulse signal of the control inverter is formed through the input reference voltage and phase angle of the PWM generator.

4 Conclusion

Photovoltaic power generation will become one of the most important means of obtaining energy in the 21st century. Improving the energy utilization efficiency of photovoltaic power generation in microgrids and developing operational control strategies for microgrids are two important research directions with significant practical value. The conclusions drawn from the experimental research in this article are as follows:

In the analysis of the transfer of movable loads, during the 13th to 22nd hour period, the peak-to-valley difference of movable loads in the classical two-stage robust optimization model and the model proposed in this paper were 69.32 MW and 49.14 MW, respectively. The peak-to-valley difference in this paper's model is smaller than that in the classical two-stage robust optimization model, and the slope of the load curve is more gradual. This verifies that the movable loads in this paper's model have stronger mobility and superior peak-shaving and valley-filling capabilities compared to traditional models, effectively reducing the difficulty of peak regulation in the system.

In the analysis of maximum power tracking output characteristics under four environmental conditions, it was found that the maximum power value tracked by the algorithm in this paper under Environment 3 was 851.9W, with an error of only 0.25W compared to the actual maximum power. This demonstrates the convergence of the algorithm in this paper for global maximum power tracking.

Funding

This work was supported by Key Technology Research on Virtual Power Plant for Multi-Participant Cooperative Game in Distributed Energy under Yunnan Province Key Research and Development Program (202302AF080006) and Key Technology Research on Cooperative Operation of Virtual Power Plant for Multi-Participant Cooperative Game under Innovation Project of China Southern Power Grid Co., Ltd. (YNKJXM20240065).

About the Author

Xiran Zhang (1995.05), male, Han Nationality, from Qujing, Yunnan Province, Master of Leeds University, engineer, engaged in the research and application of new load management system technology.

Xuehao He (November 1994), male, Naxi nationality, from Lijiang, Yunnan province, holds a doctorate degree from North China Electric Power University. He is a senior engineer engaged in research and application of active distribution network and demand side response technology.

Yiran Rao (1993.05) male, Han nationality, from Shenzhen, Guangdong province, bachelor's degree from University of California, Berkeley. His research interests include virtual power plant, distribution side and electricity information acquisition and monitoring.

Jiaquan Yang (born in January 1978), male, Han Nationality, from Kunming, Yunnan Province, has a master's degree from Xi' an Jiaotong University. He is a senior engineer engaged in the research and application of smart grid and new power system technology.

Junyu Liang (born in October 1983), male, Han Nationality, born in Honghe, Yunnan Province, has a doctorate degree from North China Electric Power University and is a senior engineer. He is engaged in the research and application of active distribution network and demand side response technology.

References

[1] Das, U. K., Tey, K. S., Seyedmahmoudian, M., Mekhilef, S., Idris, M. Y. I., Van Deventer, W., ... & Stojcevski, A. (2018). Forecasting of photovoltaic power generation and model optimization: A review. Renewable and Sustainable Energy Reviews, 81, 912-928.

[2] Chen, Y., He, L., & Li, J. (2017). Stochastic dominant-subordinate-interactive scheduling optimization for interconnected microgrids with considering wind-photovoltaic-based distributed generations under uncertainty. Energy, 130, 581-598.

[3] Kumar, R., & Singh, S. K. (2018). Solar photovoltaic modeling and simulation: As a renewable energy solution. Energy Reports, 4, 701-712.

[4] Gruosso, G., & Maffezzoni, P. (2020). Data-driven uncertainty analysis of distribution networks including photovoltaic generation. International Journal of Electrical Power & Energy Systems, 121, 106043.

[5] Putra, J. T., & Setyonegoro, M. I. B. (2024). Modeling of high uncertainty photovoltaic generation in quasi dynamic power flow on distribution systems: A case study in Java Island, Indonesia. Results in Engineering, 21, 101747.

[6] Zhang, F., Wang, X., Wang, W., Zhang, J., Du, R., Li, B., & Liu, W. (2023). Uncertainty

analysis of photovoltaic cells to determine probability of functional failure. Applied Energy, 332, 120495.

[7] Yao, H., Qin, W., Jing, X., Zhu, Z., Wang, K., Han, X., & Wang, P. (2022). Possibilistic evaluation of photovoltaic hosting capacity on distribution networks under uncertain environment. Applied Energy, 324, 119681.

[8] Nasrollahi, M., Arandian, B., & Baharizadeh, M. (2022). Robust optimum distribution network scheduling with distributed generations, electric vehicles, and storage units. International journal of energy research, 46(7), 9431-9443.

[9] Pierro, M., De Felice, M., Maggioni, E., Moser, D., Perotto, A., Spada, F., & Cornaro, C. (2018). Photovoltaic generation forecast for power transmission scheduling: A real case study. Solar Energy, 174, 976-990.

[10] Samantaray, S., & Kayal, P. (2023). Capacity assessment and scheduling of battery storage systems for performance and reliability improvement of solar energy enhanced distribution systems. Journal of Energy Storage, 66, 107479.

[11] Ying, Y., Wu, Y., Su, Y., Fu, R., Liang, X., & Xu, H. (2017). Dispatching approach for active distribution network considering PV generation reliability and load predicting interval. The Journal of Engineering, 2017(13), 2433-2437.

[12] Chen, Y., Strothers, M., & Benigni, A. (2018). All-day coordinated optimal scheduling in distribution grids with PV penetration. Electric Power Systems Research, 164, 112-122.

[13] Kumar, K. P., & Saravanan, B. (2017). Recent techniques to model uncertainties in power generation from renewable energy sources and loads in microgrids–A review. Renewable and Sustainable Energy Reviews, 71, 348-358.

[14] Ma, Y., Dong, X., Yang, P., Liu, Z., Wang, Y., & Lu, T. (2023). Robust optimization model of flexible distribution network considering source-load uncertainty. Electric Power Systems Research, 223, 109698.

[15] Yan, Y., Huang, C., Guan, J., Zhang, Q., Cai, Y., & Wang, W. (2024). Stochastic optimization of solar-based distributed energy system: An error-based scenario with a day-ahead and real-time dynamic scheduling approach. Applied Energy, 363, 123099.

[16] Lee, C. Y., & Tuegeh, M. (2020). Optimal optimisation-based microgrid scheduling considering impacts of unexpected forecast errors due to the uncertainty of renewable generation and loads fluctuation. IET Renewable Power Generation, 14(2), 321-331.

[17] Li, Z., Ye, H., Li, Y., Li, J., Zhou, H., & Yang, Y. (2024, November). Optimal Source-Load-Storage Day-Ahead Scheduling Considering Source and Load Uncertainties. In 2024 IEEE 8th Conference on Energy Internet and Energy System Integration (EI2) (pp. 1627-1632). IEEE.

[18] Li, Z., & Zhang, Z. (2021). Day-ahead and intra-day optimal scheduling of integrated energy system considering uncertainty of source & load power forecasting. Energies, 14(9), 2539.

[19] Prusty, B. R., & Jena, D. (2017). A critical review on probabilistic load flow studies in uncertainty constrained power systems with photovoltaic generation and a new approach. Renewable and Sustainable Energy Reviews, 69, 1286-1302.

[20] Liu, S., Liu, P. X., Wang, X., Wang, Z., & Meng, W. (2017). Effects of correlated photovoltaic power and load uncertainties on grid-connected microgrid day-ahead scheduling. IET Generation, Transmission & Distribution, 11(14), 3620-3627.

[21] Alzahrani, A., Hafeez, G., Ali, S., Murawwat, S., Khan, M. I., Rehman, K., & Abed, A. M. (2023). Multi-objective energy optimization with load and distributed energy source scheduling in the smart power grid. Sustainability, 15(13), 9970.

[22] Hou, J., Yu, W., Xu, Z., Ge, Q., Li, Z., & Meng, Y. (2023). Multi-time scale optimization scheduling of microgrid considering source and load uncertainty. Electric Power Systems Research, 216, 109037.

[23] Yin, H., Wang, Y., Wu, G., Liu, Y., Chen, Y., & Liu, J. (2024). Distributed optimal operation of PV-storage-load micro-grid considering renewable and load uncertainties. Journal of Energy Storage, 86, 111168.

[24] Yu, H., Ye, C., Li, S., Wang, H., Bian, J., & Li, J. (2025). Multi-Timescale Optimization Scheduling of Distribution Networks Based on the Uncertainty Intervals in Source-Load Forecasting. Energy Engineering, 122(6).

[25] Tan, M., Li, Z., Su, Y., Ren, Y., Wang, L., & Wang, R. (2024). Dual time-scale robust optimization for energy management of distributed energy community considering source-load uncertainty. Renewable Energy, 226, 120435.

[26] Dong, H., Li, S., Dong, H., Tian, Z., & Hillmansen, S. (2020). Coordinated scheduling strategy for distributed generation considering uncertainties in smart grids. IEEE access, 8, 86171-86179.

[27] Li, D., Zong, Y., Lai, X., Huang, H., Zhao, H., & Dong, S. (2023). Chance-Constrained Dispatching of Integrated Energy Systems Considering Source–Load Uncertainty and Photovoltaic Absorption. Sustainability, 15(16), 12459.

[28] Li, Y., Yang, Z., Li, G., Zhao, D., & Tian, W. (2018). Optimal scheduling of an isolated microgrid with battery storage considering load and renewable generation uncertainties. IEEE Transactions on Industrial Electronics, 66(2), 1565-1575.

[29] Xie Ying. (2025). A Study of Energy-Efficient Routing Protocols for Industrial IoT WSNs Combining GA and ACO Algorithms. International Journal of High Speed Electronics and Systems,(prepublish).

[30] Kangrui Liu,Ming Li,Sizhe Chen,Jiashun Qu & Ming’ou Zhou. (2025). Research on deep learning decoding method for polar codes in ACO-OFDM spatial optical communication system. Optoelectronics Letters,21(7),427-433.